Dynamical Characterization of a Low Oxygen Submesoscale Coherent Vortex in the Eastern North Atlantic Ocean

Alice Pietri, J. Karstensen

HAL Id: hal-01832854

https://hal.science/hal-01832854

Submitted on 4 Jan 2022

RESEARCH ARTICLE

Dynamical Characterization of a Low Oxygen Submesoscale Coherent Vortex in the Eastern North Atlantic Ocean

A. Pietri[1,2] and **J. Karstensen[1]**

[1]GEOMAR Helmholtz Centre for Ocean Research Kiel, Kiel, Germany, [2]Now at LOCEAN-IPSL, UPMC, Paris, France

Abstract A submesoscale coherent vortex (SCV) with a low oxygen core is characterized from underwater glider and mooring observations from the eastern tropical North Atlantic, north of the Cape Verde Islands. The eddy crossed the mooring with its center and a 1 month time series of the SCV's hydrographic and upper 100 m currents structure was obtained. About 45 days after, and ∼100 km west, the SCV frontal zone was surveyed in high temporal and spatial resolution using an underwater glider. Satellite altimetry showed the SCV was formed about 7 months before at the Mauritanian coast. The SCV was located at 80–100 m depth, its diameter was ∼100 km and its maximum swirl velocity ∼0.4 m s^{-1}. A Burger number of 0.2 and a vortex Rossby number 0.15 indicate a flat lens in geostrophic balance. Mooring and glider data show in general comparable dynamical and thermohaline structures, the glider in high spatial resolution, the mooring in high temporal resolution. Surface maps of chlorophyll concentration suggest high productivity inside and around the SCV. The low potential vorticity (PV) core of the SCV is surrounded by filamentary structures, sloping down at different angles from the mixed layer base and with typical width of 10–20 km and a vertical extent of 50–100 m.

1. Introduction

Submesoscale coherent vortices (SCV) are isolated, long-lived baroclinic eddies, typically having spatial scales smaller than mesoscale eddies. They are usually anticyclonically rotating, show a stratification, and thus potential vorticity (PV), minimum in the center, and show a subsurface velocity maximum (McWilliams, 1985, 2016). SCVs in the thermocline are also called intra-thermocline eddies or Anticyclonic Modewater eddies. SCVs are very efficient in transporting heat, salt, and biogeochemical properties in the upper ocean (Chaigneau et al., 2011; Chelton et al., 2011; Schütte et al., 2016a; Zhang et al., 2013).

Our understanding of the full 3-D structure of mesoscale eddies in general is still rather limited and confined mostly to modeling studies. In situ observations of sufficient horizontal and vertical resolution are sparse and satellite data only gives information on their surface manifestation. Recent studies have highlighted the important impact submesoscale structures (O(1–10 km)) that develop in the vicinity of eddies can have on the shape and dynamics of such mesoscale vortices (e.g., Godø et al., 2012; Klein & Lapeyre, 2009; McWilliams, 2016; Meunier et al., 2015; Karstensen et al., 2017). On the outskirt of eddies elongated filaments in the vertical plane have been observed with a height in the order of some tens of meters and horizontal scales of about 1–10 km (Karstensen et al., 2017; Ledwell et al., 1993) and crossing isopycnals. Such filaments have been associated with submesoscale circulations which ultimately may contribute to the decay of the mesoscale structures (Armi et al., 1988) or may transfer energy to the mesoscale flows (Molemaker et al., 2015).

The SCVs contain in their PV minimum rather homogeneous water with low stability and show a depression of the pycnocline underneath the weakly stratified core (as anticyclonic eddies show) and a shoaling of the pycnocline above it (as cyclonic eddies show) (d'Asaro, 1988; McWilliams, 1985). When considering satellite altimeter data only, SCVs often cannot be distinguished from other anticyclonically rotating (positive sea level anomaly) eddies. As such global and regional statistical analysis of eddies do not specifically disclose them (e.g., Chaigneau et al., 2011; Chelton et al., 2011a; Zhang et al., 2013). For the eastern tropical North Atlantic SCVs have been found to play an important role in the redistribution of properties from the eastern boundary upwelling region into the open ocean (Schütte et al., 2016a). Based on a combination of in situ

profile and satellite data, Schütte et al. (2016a) could show that SCVs in the eastern tropical North Atlantic are exceptional as they are characterized by a cold SST, in contrast to normal anticyclones that show warm SST anomalies (e.g., Joyce et al., 2013). This observation enabled a statistical assessment of occurrences and characteristics of SCVs for the region. Although only 10% of all eddies where SCVs they contributed about the same amount of heat and salt transport from the coast into the open ocean as the cyclonic eddies which where 50% of all eddies detected. Recently a global analysis of sea level anomaly in combination with Argo data searched specifically SCVs and found them in all oceanic areas but given the inhomogeneity of the Argo data in space and time a statistical assessment of SCVs occurrence was not possible (Zhang et al., 2017).

SCVs with a low PV core at shallow depth, close to the euphotic zone, have been found very productive even in generally low-productivity areas, such as the subtropical North Atlantic (Karstensen et al., 2015; McGillicuddy et al., 2007). High productivity was also linked to unexpected low oxygen concentrations and the creation of open ocean "dead-zones" (Karstensen et al., 2015). The high productivity has been accounted to an enhanced vertical flux of nutrient-rich deep water into the sunlit upper ocean and associated with the dynamics of SCVs. McGillicuddy et al. (2007), based on idealized studies (Dewar & Flierl, 1987), proposed a local upwelling mechanism across anticyclonic eddies that is driven from an Ekman transport divergence due to the meridional difference in wind stress across the vortex. Karstensen et al. (2017) proposed a local upwelling scheme based on submesoscale dynamics related to the propagation of near-inertial internal waves (NIW) at the outskirt of the SCV that create an erosion of the low PV core. In Gulf Stream rings, which are normal anticyclonic eddies, intense mixing have been reported inside the ring and associated with the downward propagation and breaking of possibly trapped NIWs (e.g., Kunze et al., 1995).

The formation of SCVs from poleward undercurrent in eastern boundary regions is well documented (e.g., Armi & Zenk, 1984; Colas et al., 2012; Garfield et al., 1999; Pingree & Le Cann, 1992). They have been shown to originate from regions of intense instability where the current separates from the continental slope (Molemaker et al., 2015). The SCVs propagate westward but maintain relatively constant core properties, indicating weak impact of lateral mixing with surrounding water (Armi et al., 1988; Fukumori, 1992; Joyce & McDougall, 1992; Karstensen et al., 2017). Because observations of SCVs in the open ocean are sparse, little information exists about the temporal evolution and final erosion of those eddies. Here we describe one particular well-surveyed low oxygen SCV observed in early 2010 with a mooring and a glider several month after its formation off the coast of Mauritania. After a short introduction into the observational data a dynamical characterization of the eddy will be done. By merging the data sets from the mooring and the glider the mesoscale and submesoscale variability is described in section 3. In section 4, we discuss the dynamics associated with the SCV and in section 5 concluding remarks are given.

2. Data and Methods

2.1. Mooring

The Cape Verde Ocean Observatory (CVOO) mooring is located at about 17°36.4′N and 24°14.98′W in 3600 m deep water in the eastern North Atlantic Ocean (black star in Figure 1). The mooring location is approximately 60 km northeast of the Cape Verde island Sao Vicente. We report here on data that was recorded during the mooring deployment period from October 2009 to May 2011 (KPO_1041). In total, 17 MicroCat CTD sensors were installed and sampled every 30 min, with eight of them in the upper 300 m. In the upper 60 m, the CTD sensors were spaced by 10–15 m. A 300 kHz upward looking Acoustic Doppler Current Profiler (ADCP) was installed at 107 m depth and resolved in 4 m depth cells the upper layer flow field with 1 h temporal resolution. Two Aanderaa oxygen optodes (Type 3830), installed at 42 and 170 m depth, recorded oxygen relevant parameters (phase, temperature) every 2 h.

Typically the currents are sluggish in the region and as such the mooring stood upright and instruments moved only a few meters in the vertical. However, during the strong flow event associated with the SCV's passage, the upper instruments were pushed downward as much as 150 m. Not all instruments were equipped with pressure sensors but pressure (and thus depth) information was needed. Therefore, a pressure matrix was created for all instruments, which was inferred from the observed pressure variability (some instruments) and extrapolated for the instruments without a pressure sensor through linear interpolation. After allocating a pressure value to all instruments the salinity was calculated from the conductivity (where
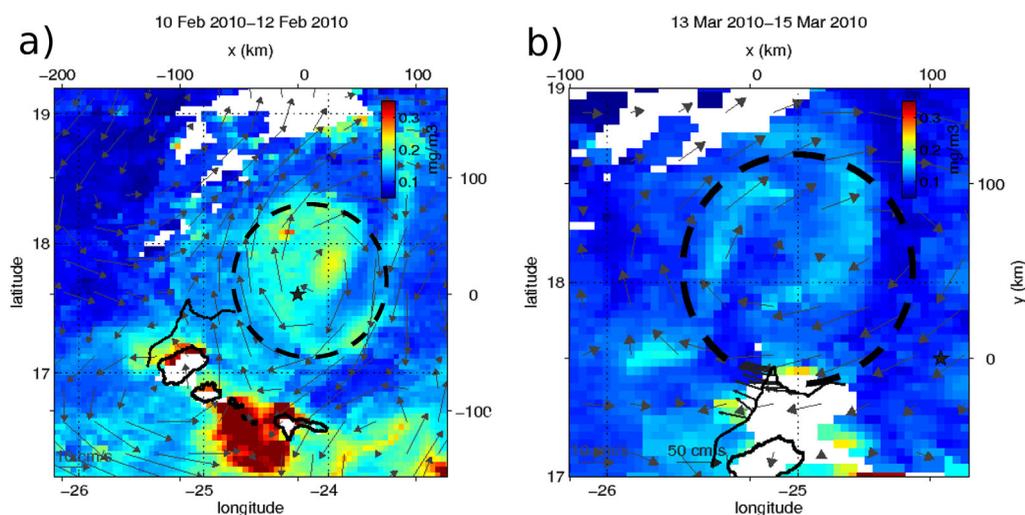
Figure 1. Chlorophyll concentration (mg m^{-3}) averaged for (a) 10–12 February when an anticylconic eddy passed the mooring CVOO (black star located at 17.61°N, 24.25°W) and (b) 13–15 March a few days before it was sampled by a glider (black line). The dark gray vectors represent the geostrophic velocity derived from satellite altimetry and the black vectors along the glider track the glider depth-averaged velocity. The black dashed circles outline the position of the eddy on each date.

available). The general MicroCat CTDs quality was assessed against calibrated shipboard CTD during the deployment and the recovery cruises. To do so, the MicroCats were mounted to the CTD rosette and at depth with low vertical salinity and temperature gradients the CTD was stopped for several minutes and the data later compared. For the purpose of this analysis the temperature, salinity, and velocity data from the mooring were filtered with a 24 h running average in order to remove tides and perturbations with short time scale.

2.2. Satellite Data

Sea level anomaly (SLA) maps were used to detect and track the eddy before and after it passed the CVOO mooring near the Cape Verde Islands. The SLA fields were provided by AVISO (Archiving, Validation, and Interpretation of Satellite Oceanographic http://www.aviso.oceanobs.com/). The data used is a weekly merged multisatellite product projected on a grid with a 1/3° horizontal resolution.

The wind fields are obtained from the Centre de Recherche et d'Exploitation Satellitaire (CERSAT), at IFREMER, Plouzané (France). They are gridded products from Metop/ASCAT scatterometer retrievals and produced over global ocean with a spatial resolution of 0.25° and a daily temporal resolution (Bentamy & Croize-Fillon, 2011).

The Chlorophyll surface concentration was provided by ACRI-ST—GlobColour. It consists in a daily product merged from SeaWIFS, MERIS, and MODIS with a 4 km horizontal resolution. The maps were averaged over three days to best represent the chlorophyll concentration spatial patterns despite the missing data due to cloud coverage (see Figure 1).

2.3. Glider

We will make use of the data from an autonomous electric underwater SLOCUM Web Research G1 glider (Ifm11). The glider was deployed on 12 March 2010, as part of a local survey (in collaboration with five other gliders) around the CVOO mooring. The Ifm11 glider was equipped with an unpumped SeaBird CTD, an oxygen optode 3830 (similar to the instruments deployed at the CVOO mooring) and a Wetlabs optical fluorometer/turbidity sensor (ECO-PUCK). The glider sampled sea-saw shape slanted profiles with an approximate 1:1 distance/depth ratio of 500 m/500 m. Starting with different depth at the beginning of the mission (data not used here), from 16 March to the end of its deployment the glider dived to 500 m depth. The conductivity was corrected as outlined in Garau et al. (2011) before salinity was derived. The optode was calibrated by mounting it on a CTD rosette and comparing the Winkler calibrated Clarke Sensors (SBE43) with the optode records (see Hahn et al., 2014). The fluorometer/turbidity data were not calibrated

for our purpose. The glider was deployed south of the island Sao Vicente from a local fishing boat. To reach the CVOO mooring, Ifm11 (as the other gliders) was navigated first upwind (west) of Santo Antao island followed by a Northeast course (Figure 1). During the Northeast course, the glider recorded on 16 March 2010 suddenly very low oxygen at about 60 m depth and significantly slowed down in forward speed. The lowest oxygen records were less than $\sim$10 μmol kg^{-1} and much lower than previously reported lowest oxygen concentrations for the region ($\sim$40 μmol kg^{-1}; Stramma et al., 2008). The anomalous oxygen signal was surveyed until 22 March 2010. However, the glider then continued for its core mission around the CVOO mooring. After recovery of the mooring in May 2011, it became clear that the glider sampled a low oxygen SCV that was also sampled with the CVOO mooring about a month before the glider survey (Karstensen et al., 2015).

Geostrophic velocities perpendicular to the glider tracks were calculated by applying a 40 km Gaussian window ($\sim$80 h at the glider speed) to the density data to remove high-frequency variability and then using the thermal wind balance with the depth-averaged velocity as obtained by the dead reckoning of the glider as a reference (Pietri et al., 2013, 2014; Todd et al., 2009).
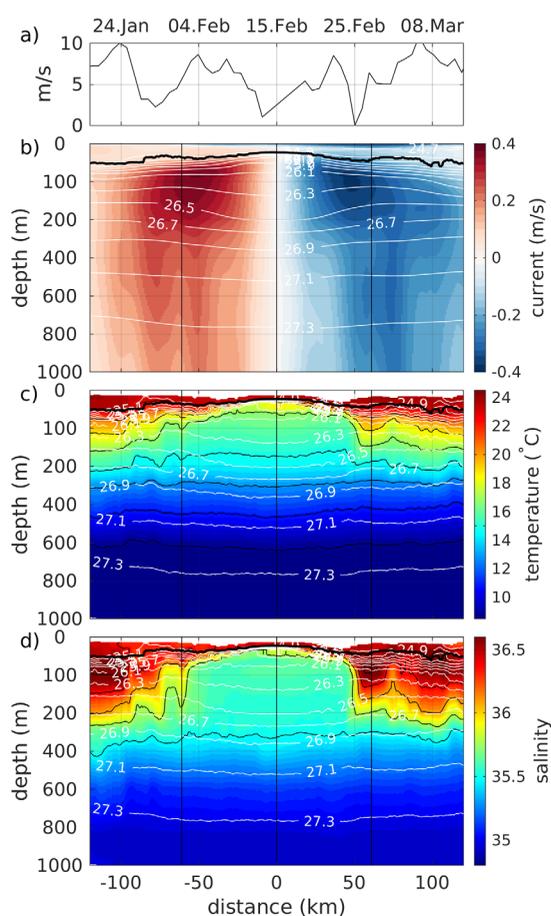

Figure 2. (a) Wind speed (m s^{-1}) at the mooring site from 20 January 2010 to 12 March 2010. (b) Azimuthal velocity. The upper part (0–100 m depth) shows direct observation of the current, below (100–200 m depth) the velocity are derived from the thermal wind balance referenced to the observed current at $\sim$95 m. (b) Temperature and (c) salinity during the passage of the eddy. The distance from the center of the eddy is calculated from the eddy drift speed estimated in section 3.1. White lines are selected density contours (filtered in Figure 2b) and unfiltered in Figures 2c and 2d. The thick black line shows the depth of the mixed layer. Vertical black lines are plotted every 13 days and indicate the number of full rotations carried out by the eddy. Note that the vertical scale is not linear and highlights the 0–200 m part.

3. Structure of the SCV

3.1. Surface Manifestation

Anticyclonic SCVs generate a positive sea level anomaly on altimetry maps that can be identified and tracked in order to derive a propagation speed. The SLA reveals an anomaly of about +10 cm in February/March 2010 at the CVOO mooring site. This positive SLA anomaly goes along with a region of enhanced chlorophyll-a concentration (Figure 1). On 10–12 February, a region of relatively high chlorophyll concentration can be observed close to the eddy center (Figure 1a). It unfolds into a filament-like shape in the center and around the eddy. A month later (Figure 1b) patches of relatively high chlorophyll concentration can still be observed in the eddy region (now about 100 km further west). High productivity in mode water eddies has been previously observed and related to upwelling of nutrient-rich water within the eddy (e.g., Ledwell et al., 2008; Karstensen et al., 2017; McGillicuddy et al., 2007).

Tracking the SLA anomaly back in time reveals an eddy formation in July 2009 off the coast of Mauritania (18°N/16.5°W) and a tracking after the passage at the CVOO indicates the SCV may have decayed at about 35°W about 15 month after its formation, in October 2010. The linear fit to the time/space domain results in a mean propagation speed of about 3.5 km d^{-1} between the coast and 25°W (CVOO) and about 5.7 km d^{-1} after. On average, the SCV traveled at a speed of $\sim$4.5 km d^{-1}. Using consecutive SLA maps to track the displacement of the maximum SLA, we found a propagation speed of about 4 $\pm$ 2 km d^{-1} during the mooring passage (21 January to 18 March 2010).

In the mooring records, the passage of the SCV is easily identified from the ADCP velocity data (Figure 2b). The meridional flow reverses sign, from Northward to Southward velocities, which is typical for an anticyclonic eddy traveling westward. Creating a polar coordinate plot of the observed eastward versus northward velocity time series averaged between 40 and 100 m depth and color coding salinity to it (hodograph, Figure 3) reveals the specific hydrographic structure, namely low salinity in the eddy core. An eddy moving past a mooring will produce different features on the hodograph depending on how close the mooring was from the center (Lilly & Rhines, 2002): the closer the observations (mooring) where taken to the center of the
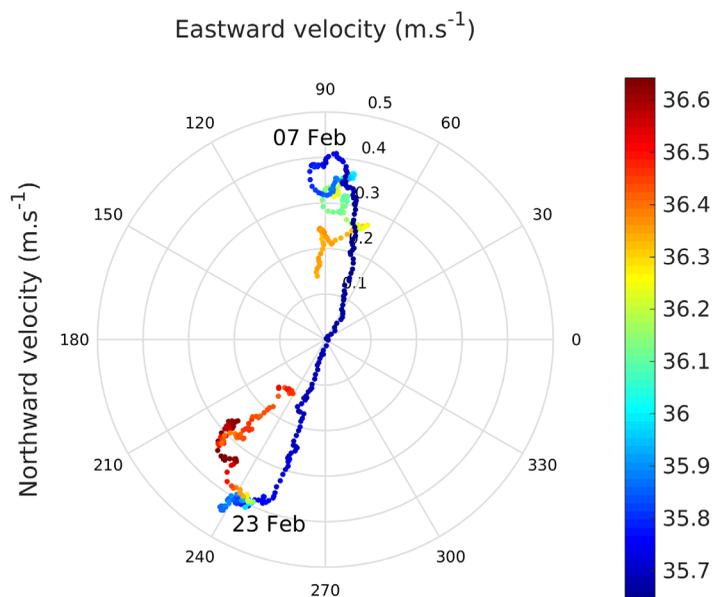
Figure 3. Hodograph of the observed currents averaged between 40 and 100 m depth for the period 26 January to 6 March 2010. The color corresponds to the salinity averaged between 40 and 100 m depth. The two dates correspond to the occurrence of the strongest northward and southward velocities.

eddy the more the hodograph unfolds into a straight line. In our case, within the salinity anomaly, the hodograph tends to be a straight line, which indicates that the core of the eddy has crossed the mooring.

It is possible to estimate the SCV drift speed from knowledge about the two-dimensional velocity structure of the eddy (Lilly & Rhines, 2002). Assuming the eddy drift does not vary with depth, the observed speed can be separated into an azimuthal speed and a translation speed, which are perpendicular to each other on a cross section passing through the eddy center along the propagation direction. The eddy drift speed (U_d) and direction can be estimated from the velocity field observed at the mooring location. The edges of the eddy core are defined by the local maxima in velocity. Those maxima, V_{1max} at time t_1 and V_{2max} at time t_2 allow to identify $\Delta t = t_2 - t_1$, the time period during which the eddy is passing by the mooring site. The eddy translation direction is then perpendicular to the vector difference $V_{2max} - V_{1max}$ (Fan et al., 2013; Lilly & Rhines, 2002) and its velocity can be observed at the time where the azimuthal velocity is null.

Using the moored ADCP data averaged between 40 and 100 m depth, where the maximum velocity is observed, V_{1max} and V_{2max} have been located and the direction of propagation identified as Northwest. To infer the translation speed, the velocity recorded by the ADCP in the direction of propagation was filtered with a 90 days wide Hanning window (3 times the duration of the eddy), averaged between 40 and 100 m depth and over the core of the eddy (Lilly et al., 2003). The obtained speed is ~4.6 km d^{-1} which is very close to the drift velocity estimated from the altimetry data, thus adding confidence in the value. Note that the estimated eddy size will tend to appear smaller if the SCV center did not exactly crossed the mooring. In the rest of the paper, we will refer to the azimuthal velocity, that is to say the velocity perpendicular to the direction of propagation.

During the passing of the eddy, surface winds were blowing in the Southwest direction with an averaged speed of 5 m s^{-1}. From 20 January to 12 March, the wind intensity varies with a period of about 13 days and several relatively high wind episodes were observed on 24 January, 4 February, 23 February, and 7 March ranging from 8.5 to 10.8 m s^{-1} (Figure 2a).

3.2. Vertical Structure

Once the propagation speed is known, the spatial structure of the eddy and its radius can be estimated. The temperature, salinity, and density fields recorded by the moored instruments (Figures 2c and 2d) show the SCV as a cold and fresh lens of water. The eddy's radius is ~50 km and it has a large vertical extent with density anomalies visible up to 1,500 m depth (not shown here). The eddy passage goes along with the rising of the mixed layer base from ~50 m depth to ~20 m depth (Figure 2). The eddy core, from mixed layer base to about 200 m depth, is characterized by weak stratification (low PV) as typical for SCVs.

Direct information about the velocity structure of the water column from surface to 100 m depth is obtained from the ADCP data. The circulation below 100 m is calculated from the thermal wind balance applied to the observed density field, filtered with a 40 km running mean, and referenced to the observed ADCP current at 95 m (Figure 2b). The current during the passing of the eddy is characteristic of a SCV, with a general anticyclonic spin and a maximum velocity located in the subsurface. Here maximum velocities of ~0.4 m s^{-1} on both side of the eddy are located at ~80 m depth and ~50 km from the eddy center. The maximum swirl velocity marks the depth where isopycnal surfaces are domed upward, while below they slope downward as expected for a SCV. A full rotation thus takes about 13 days to be completed at the velocity maximum, which means the eddy did two full rotations while passing by the mooring site (Figure 2).

The water mass inside the eddy low PV core has a narrow temperature range of ~16°C and salinity of ~35.6 (Figure 4). This water mass indicates South Atlantic Central Water (SACW) origin, typically found at the Mauritanian shelf, and is very distinct from the warmer and more saline North Atlantic Central Water (NACW)
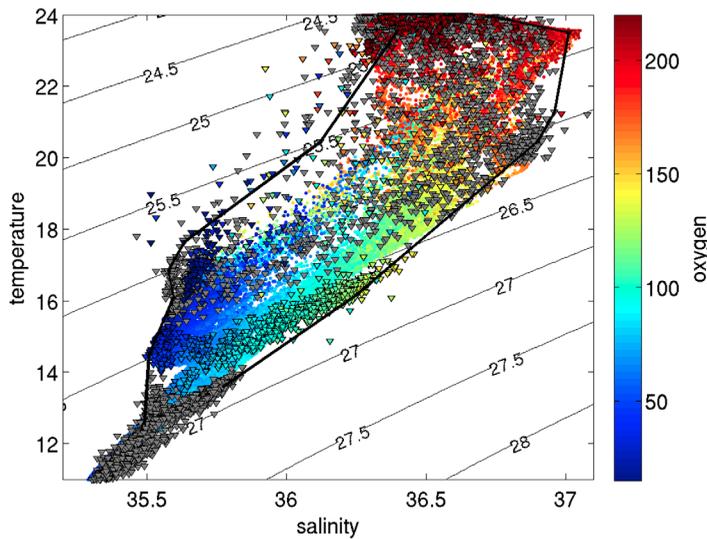
Figure 4. *T/S* diagram of the mooring and the glider data. Color indicates the oxygen concentration [μmol L^{-1}]. Triangles indicate the mooring data (gray where there is no oxygen data) and circles the glider data. Black lines show the characteristics *T/S* profiles inside and outside of the eddy.

character in the surrounding water (Karstensen et al., 2015; Schütte et al., 2016b). Another striking difference between the water in the center of the eddy and the surrounding water is the oxygen concentration. The two optodes located at ~40 and ~170 m depth recorded a large drop in dissolved oxygen concentration during the eddy passage, with concentration close to zero at the upper sensor (Karstensen et al., 2015).

Outside of the low PV core different transition zones are observed. A frontal region outward from the maximum velocity shows strong horizontal gradients in salinity and temperature. Thermohaline structures with a horizontal scale of (O 10 km) and a vertical extension of up to 300 m can be observed framing the core of the SCV in the transition zone (Figures 2c and 2d). In particular the salinity field exhibits elongated structures at −60 and −75 km and between 100 and 300 m depth (Figure 2c).

3.3. Characteristics of the Flow

To describe the dynamics of the eddy, a set of nondimensional characteristic numbers has been estimated. First, the Burger number expresses the relative importance of stratification and rotation to the flow field:

$$Bu = \left(\frac{NH}{fL}\right)^2,$$

where $N^2 = -g/\rho_0\, \partial_z \rho$ is the Brunt-Väisälä or buoyancy frequency. The Coriolis parameter, $f = 4.4 \times 10^{-5}$ s^{-1}, is kept constant in all calculations. The horizontal length scale of the eddy corresponds to its diameter ($L = 100$ km) and the vertical scale is defined as the thickness of its core ($H = 400$ m) (D'Asaro et al., 1994; Hebert et al., 1990). The value of the Burger number is then $Bu \sim 0.2$, which indicates a flat lens (note that the Bu is even smaller if only the low PV core thickness is used for the calculations). This number is comprised within the stability bounds for SCVs defined by McWilliams (1985) as $0.05 < Bu < 1$.

The internal deformation radius ($Rd = NH/f$) is 45 km, a value very close to the eddy radius. This differs from McWilliams's (1985) definition of SCVs as features smaller than the first baroclinic radius of deformation but is not inconsistent with previous observations of SCVs. In fact occurrences of SCVs with deformation radius similar or larger to the local eddy radius have been reported in several regions (e.g., Bosse et al., 2015; Hormazabal et al., 2013; Pelland et al., 2013).

The vortex Rossby number ($vRo = V_{max}/(R_{max} * f)$) assesses the ratio of the centrifugal force to the Coriolis force. The eddy vRo is ~0.15 which indicates that the centrifugal force is small compared to the planetary vorticity and the eddy circulation is close to the geostrophic balance. Although the Burger and vortex Rossby number suggest the eddy is stable and in geostrophic balance, the dynamics of the flow is very variable along the eddy radius. In fact, the Rossby number, $Ro = \zeta/f$ in the center of the eddy can reach up to 0.3 (Figure 5a).

The Richardson number (Ri) is a measure of the baroclinicity of the vortex. It is expressed as the ratio of the vertical shear of buoyancy over the vertical shear of horizontal velocity:

$$Ri = \frac{\partial b/\partial z}{(\partial v/\partial z)^2},$$

Figure 5. (a) Rossby number (black contours at ±0.1), (b) Richardson number (plotted on a log scale, contour at $Ri = 10$) derived from the mooring data from 20 January to 12 March 2010. White lines are selected density contours. The thick black line shows the depth of the mixed layer. Note that the vertical scale is not linear and highlights the 0–100 m part.

where $b = -g/\rho_0 * \rho$ is the buoyancy. A low Ri indicates susceptibility to baroclinic instability, in particular, submesoscale turbulence can arise in regions of O(1) Ri. Mooring data show very few regions of O(1)
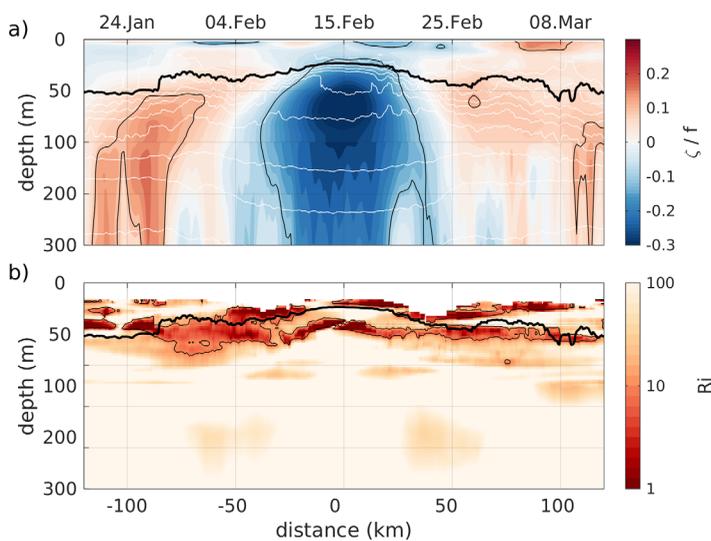
Ri (Figure 5b), and they are all located in the mixed layer. Regions of O(10) Ri can be found in the eddy core at ∼50 m depth and on the periphery, more particularly on the western side, from the mixed layer base to ∼70 m depth. Karstensen et al. (2017) showed from high-resolution ship hydrography and ADCP data that indeed critical Ri are found around the low PV core and created in NIW velocity shear regions.

A measure for the coherence of eddies, and often linked to the isolation of the water masses, is the nonlinearity expressed as the ratio of the translation speed to the rotational speed (Chaigneau et al., 2011; Flierl, 1981). Ratios exceeding 1 indicate nonlinearity and the SCV reported here has values of more than 7 times faster rotational speed along the eddy rim than the drift velocity indicating that the eddy kept a coherent structure along its path.

Note that the term SCV can be misleading when referring to a vortex close to geostrophic balance, with a radius of a few tens of kilometers, it is however widely used to describe interior anticyclones and the characteristics of this eddy compare well with previous descriptions of SCVs that followed McWilliams's (1985) first characterization. Indeed this long-lived anticyclone with dome-shaped isopycnals in its upper part and bowl-shaped in its lower part shows a middepth velocity maximum, a core of rather homogeneous water with minimum vertical stratification, strong central negative vorticity, and a Burger number within the bounds of stability for SCVs.

3.4. Fine Scale Structure on the Rim

In order to evaluate the small-scale variability at the transition between the eddy and the surrounding waters we use the high-resolution glider data for further diagnostics. The glider was directed toward the eddy center but it was pushed back out of it by the strong velocity and thus only sampled the outer part. However, the high resolution of the glider data as well as the many parameters recorded give valuable insights on the vertical structure on the boundary of this SCV.

3.4.1. Combination of the Data Sets

The distances from the eddy center are chosen as a common coordinate to compare and eventually merge the mooring and glider data as both types of observations suffer from a mix of temporal and spatial variability. At the depth of the velocity maximum a full rotation of the eddy took about 13 days to complete and thus the mooring records sampled at least two full rotations. The glider survey took place about 45 days after the mooring survey and the glider spent about 7 days in the vicinity of the eddy, as such it covered about half of the eddy periphery.

In order to position the glider dives relative to the eddy center the relative movement of the SCV during the glider survey was required. This was estimated by relocating each profile by a distance $U_d \Delta t$, with Δt the time elapsed from the first dive, in the opposite direction of propagation of the eddy. Using this corrected location, we identified the eddy center as the position where the lines perpendicular to the depth-average currents direction meet, in a similar manner as Pelland et al. (2013) and Bosse et al. (2015). Several velocity measurements, within a window of 24 h and 10 km, were selected to identify the most accurate position for the eddy center. This method allowed us to position the center 50 km away from the closest glider profile. The so obtained glider positions were then projected on two straight lines that best fitted the glider path and correspond to the two crossing of the eddy periphery (one toward the eddy and the second out of it, Figure 6).

A comparison of the thermohaline structure of the observational records from the mooring and the glider was performed. We searched for each glider T/S profile that correlated with the CVOO mooring data. To suppress short-term variability glider and mooring data were low pass filtered over a distance of 5 km (for mooring: equivalent to ∼1 day). This method showed that the glider profiles most similar to the eddy central water mass were the most northern ones, recorded on 19 March. Those profiles showed the highest correlation with the mooring profiles located 50 km from the eddy center (with a correlation coefficient higher than 0.9). This result is consistent with the position of the eddy center identified from the glider depth-averaged velocity and indicates that in 45 days the eddy did not substantially change in its dynamical and thermohaline characteristics.

To validate the derived glider track relative to the eddy center and the corresponding mooring observations, we performed a consistency check of certain data records. The depth-averaged velocity from dead reckoning of the glider was compared with the depth-averaged velocity from the combination of ADCP and
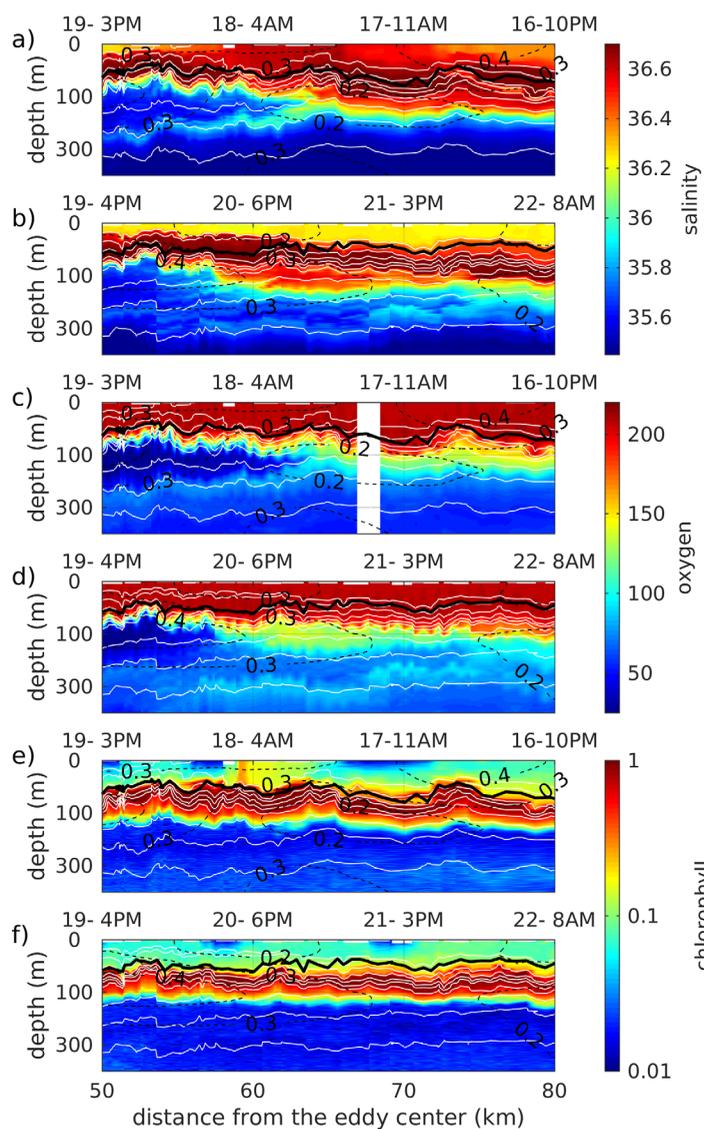
Figure 6. (a and b) Glider salinity, (c and d) oxygen (μmol L^{-1}), and (e and f) fluorescence (mg m^{-3}) data for the two crossing of the eddy rim from 16 to 22 March (the day of March and the time are indicated on top of the sections). Note that the fluorescence is plotted on a log scale. White lines represent isopycnals, black dashed lines the velocity contours and the thick black line the depth of the mixed layer. Note that the vertical scale is not linear and highlights the 0–100 m part.

geostrophy considering the respective dive depth. Figure 7a shows the norm of the mooring velocity data averaged from 0 to 500 m for both sides of the eddy and the norm of the depth-averaged velocity recorded by the glider for dives 500 m deep. The agreement suggest that, despite the fact the mooring data provides primarily the temporal evolution of the field, while the glider provides a mix of temporal and spatial variability, the inherent symmetry of the eddy does indeed permit to compare the datasets from the two different observing platforms (glider, mooring). The oxygen data, recorded at nominal 42 and 170 m depth at the mooring site during the passage of the eddy, was also compared with the glider oxygen concentrations at the same depths (Figures 7b and 7c). Again, both data sets show strong similarity with differences than can be linked with small-scale variability and with the vertical displacement of the oxygen sensor on the mooring array. As independent measurements all display significant similarity between the two platforms, the distance from the eddy center is considered a good approximation for a common coordinate.

3.4.2. Submesoscale Variability

The transition zone located between the isolated eddy center and the water mass outside is characterized in the mooring data by strong horizontal gradients and indication of frontal structures (see section 3.2). The glider data allows an observation of this region at a much higher vertical resolution. The salinity (Figures 6a and 6b) and oxygen (Figures 6c and 6d) fields both present low-aspect-ratio structures that seem to originate from the mixed layer base and slope downward at different angles and crossing isopycnals toward the rotational center of the eddy, below the low PV core and reaching depths of at least 300 m. Salty and oxygenated intrusions are observed outside of the region of maximum velocity, framing the fresh (35.5–35.8 PSU) and oxygen depleted (glider data show 20–50 μmol kg^{-1}) core of the SCV. The Chlorophyll-a fluorescence field (Figures 6e and 6f) shows high concentrations at the base of the mixed layer and a rapid decrease below. On the upper layer (0–20 m depth), several regions of apparent low chlorophyll are visible and can actually be related to daytime fluorescence quenching (Sackmann et al., 2008). Below the mixed layer, the fluorescence field does not show the same patterns as the salinity and oxygen concentration. There is however relatively high surface fluorescence on 18 March that may be related to the high chlorophyll concentration that was visible with a patchy pattern on the satellite image (Figure 1b).

From the CVOO mooring instrument records that covers the whole eddy, we have identified two typical T/S profiles for the water mass trapped inside the eddy (T_i, S_i) and for the surrounding water (T_o, S_o, Figure 4). Using the envelope curves along isopycnals, the glider T/S pairs were converted to water mass ratios D_{WM}. We use the definition

$$D_{WM} = \sqrt{\frac{(S-S_i)^2 + (T-T_i)^2}{(S_o-S_i)^2 + (T_o-T_i)^2}}.$$

A value close to 0 indicates the presence of SACW (eddy core) while 1 means a water mass more similar to NACW (surrounding waters). Figure 8 presents these ratios along the glider trajectory. Note that in the surface layer, it is not possible to differentiate the inside and outside of the SCV. At about 50–60 km from the eddy center, and between 50 and 200 m depth a region very similar to the homogeneous water mass observed for the core of the eddy from the mooring data can be found. The similarity of the T/S data
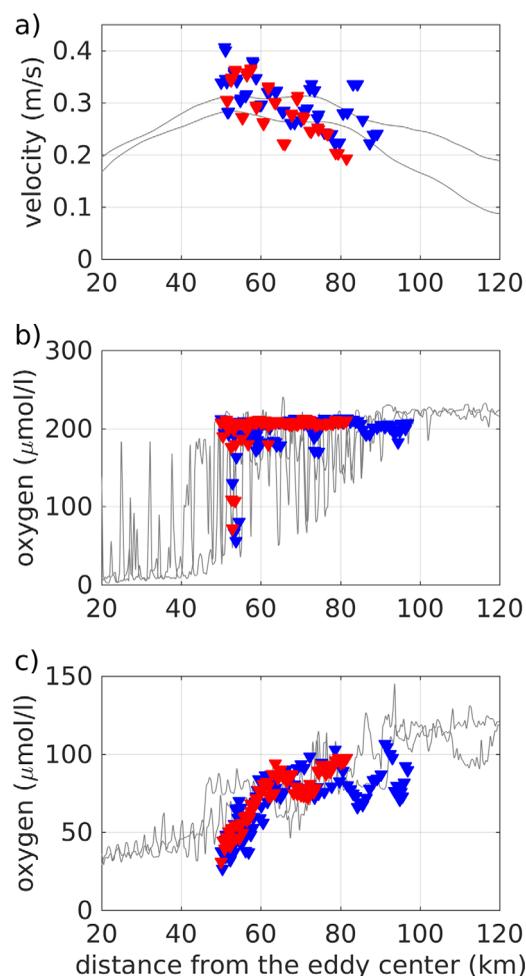
Figure 7. (a) Norm of the mooring velocity averaged from 0 to 500 m for both sides of the eddy (gray lines) and norm of the depth-averaged velocity recorded by the glider for dives 500 m deep (red and blue triangles). Oxygen concentration at ~54 m depth (b) and 182 m depth (c) recorded at the mooring site (gray lines) and measured by the glider (red and blue triangles). Red triangles correspond to the glider track entering the eddy on 15–18 March and the blue ones to the track exiting it on 19–23 March.

recorded at the mooring site and along the glider path 100 km away and more than a month later further highlights the consistency of the water mass inside the eddy. The merging however reveals a much richer T/S structure of the eddy rim, especially over the vertical, when compared with the mooring data recorded at distinct depth. From 60 to 100 km from the center, as observed on the salinity and oxygen field, elongated structures slope downward toward the eddy center reaching depths of at least 300 m (Figure 8). This layering indicates water mass interleaving and eventually lateral mixing (Joyce, 1977). In general, the glider data reveals a transition zone with a rich vertical variability surrounding the eddy while samples in the core show a very coherent and isolated structure.

The rich network of observations (satellite, mooring, glider) allows to give a multidimensionnal image of this SCVs at midlife when few observation of SCVs in the open ocean exist. Several months after its formation and before its final decay, the structure is still coherent with a low stratified core, distinct interior water mass, and oxygen concentration. Observation of filamentary structures on the outside provides valuable information on the still unresolved issue of the long-range lateral transport by SCVs in the ocean.

4. Discussion

In the past few years, a number of studies investigated the importance of submesoscale variability organized around mesoscale eddies (e.g., Brannigan, 2016; Klein & Lapeyre, 2009; Mahadevan & Archer, 2000). In particular, the presence of fine scale layered structures on the rim can impact the exchange between eddy center and surrounding water. Layering in the periphery of eddies has been observed regularly (Armi & Zenk, 1984; Pingree & Le Cann, 1993; Ruddick, 1992; Ruddick & Hebert, 1988; Ruddick & Walsh, 1994) but the processes responsible for such structures are still not clearly identified. They can be the result of internal waves breaking (Alford et al., 2016), of frontogenetic processes (Martin & Richards, 2001) or originate from meso (Smith & Ferrari, 2009) or submesoscale stirring (Shcherbina et al., 2015) of contrasted water masses. A potential role of this interleaving of water masses, as pointed out by Armi et al. (1988), is also the decay of eddies as the intrusions reach the eddy center.

The observed SCV has a low stratified core that seem to have stayed well isolated for months, with T/S characteristics very similar to the SACW found in the eastern boundary upwelling region (Schütte et al., 2016b). It exhibits very low oxygen in its core, high productivity at the surface and fine scale thermohaline interleaving on the periphery. It is still unclear what processes allow SCVs to stay isolated for such long periods of time or what brings their decay forward. Although the network of observation available does not allow to discriminate precisely what process drives the small-scale thermohaline intrusions on the rim we will present in this section a series of dynamical diagnostics that give a fuller picture of the eddy dynamics.

4.1. Secondary Ageostrophic Circulations

Fine scale thermohaline intrusions on the outskirt of eddies can be driven by frontal vertical circulations. Indeed eddies are similar to a circular density front and prone to generate horizontal and vertical gradients of the velocity and buoyancy fields that can lead to frontogenetic vertical circulations (Martin & Richards, 2001). Samuelsen et al. (2012), using numerical experiments, have shown that in an anticyclonic eddy particles tend to aggregate along the rim where then can undergo vertical displacement of up to 200 m depth both upward and downward. Such upwelling and downwelling can be related to upper layer divergence and convergence in the eddy (Zhang et al., 2015).
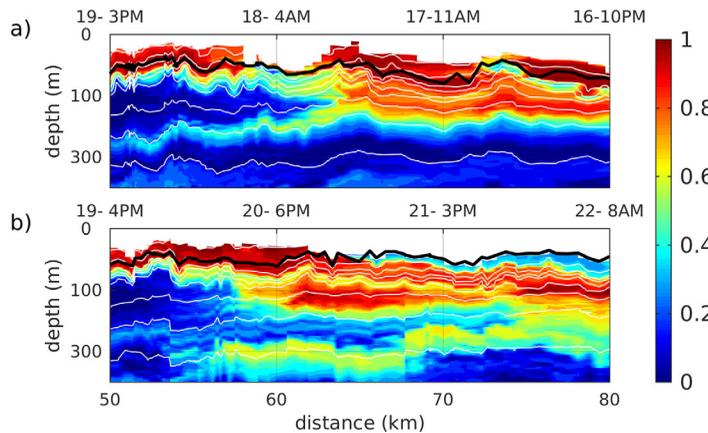
Figure 8. Similarity of the glider T/S data to the water mass inside the eddy (section 3.4.2, a value of 0 means the T/S properties over an isopycnal are similar to the water mass trapped inside the eddy and a value of 1 a similarity to the surrounding water) for the two glider crossings from 16 to 22 March 2010 (the day of March and the time are indicated on top of the sections). Whites lines represent isopycnals and the black thick line the depth of the mixed layer. Note that the vertical scale is not linear and highlights the 0–100 m part.

Brannigan (2016) also proposed symmetric instability as a process that could drive fluxes of properties between the mixed layer and the thermocline of mesoscale eddies. Indeed symmetric instability could emerge on the side of the eddy where the surface wind aligns with the direction of the flow (which would correspond to a "down-front wind" situation as described in Thomas, 2005) and generate vertical cells that would be advected by the anticyclonic circulation. Using a limiting nutrient model experiment Brannigan (2016) showed that such process could explain the radial distribution of chlorophyll concentration and its variation with time creating similar patterns as observed on satellite chlorophyll images. However, the hydrographic observations do not support the outcrop of isopycnals across the eddy which is an important boundary condition for the model proposed by Brannigan (2016).

Susceptibility to submesoscale instability can be highlighted by the distribution of potential vorticity (PV). Ageostrophic submesoscale circulations destabilize the flow and consequently create significant gradients in the PV field making it a good indicator for the presence of such instabilities. In general it has been shown that regions where the PV is close to zero or undergo a change of sign tend to present enhanced submesoscale secondary circulations (Mahadevan & Tandon, 2006; Thomas et al., 2008; Yoshikawa et al., 2001). Considering that the radial flow, u, is constant in the vertical, the potential vorticity in cylindrical polar coordinates is expressed as:

$$q = N^2 \left(f + \frac{\partial v}{\partial r} + \frac{v}{r} \right) - \frac{\partial v}{\partial z} \frac{\partial b}{\partial r},$$

where r is the distance from the eddy center. Low values of q are observed in the mixed layer of the eddy with a strong increase below, across the mixed layer base (Figure 9a). The isolated core of the SCV, below 75 m depth, is characterized by low PV values. A weak stratification, and thus small N^2 values, also generates low and even negative PV regions at ~40 m depth in the eddy center and on the left side from −120 to −80 km. Note that, in the high PV region across the mixed layer base several small-scale intrusions of negative PV are observed. Those low PV intrusions are 2–5 km wide with a vertical extent of 10 to 20 m and driven by relatively strong $\frac{\partial v}{\partial z} \frac{\partial b}{\partial r}$ values. They tend to indicate possible secondary vertical circulations across the mixed layer base. Note that they are located in a region where the wind is the opposite direction of the circular flow but could nevertheless be the remnants of former instabilities advected around the eddy.

To give more insights on the dynamics on the rim and confirm the presence of negative-PV regions with a higher resolution data set, the geostrophic PV was calculated along the glider track (Figures 10a and 10b). It also shows localized regions of negative PV across the mixed layer base, resulting from relatively high $\frac{\partial v}{\partial z} \frac{\partial b}{\partial r}$ values, at 75 km from the center on the first leg (Figure 10a) and 52 and 60 km from the center on the second leg (Figure 10b). Note that the low PV region located in the mixed layer on the first leg, around 60 km from the center, results from low stratification.

The relatively high values of PV and Ri (Figures 10a–10d) suggest that the eddy is overall symmetrically stable in the pycnocline. Although those processes are probably to account for in the upwelling of nutrients into the mixed layer they cannot explain the observed layering of the salinity and oxygen fields. However, it is interesting to note that the layering observed on the glider salinity and oxygen data
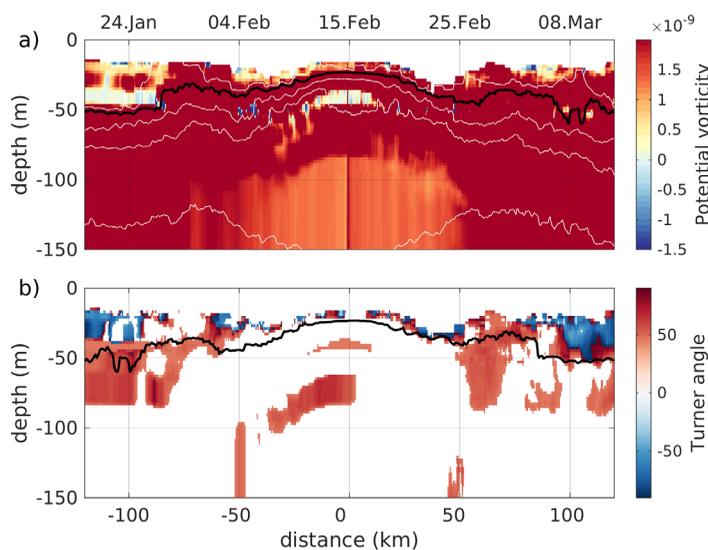

Figure 9. (a) Potential vorticity (s^{-2}) and (b) Turner angle superior to 45° and inferior to −45° derived from the mooring data from 20 January to 12 March 2010. White lines are selected density contours. The thick black line shows the depth of the mixed layer.
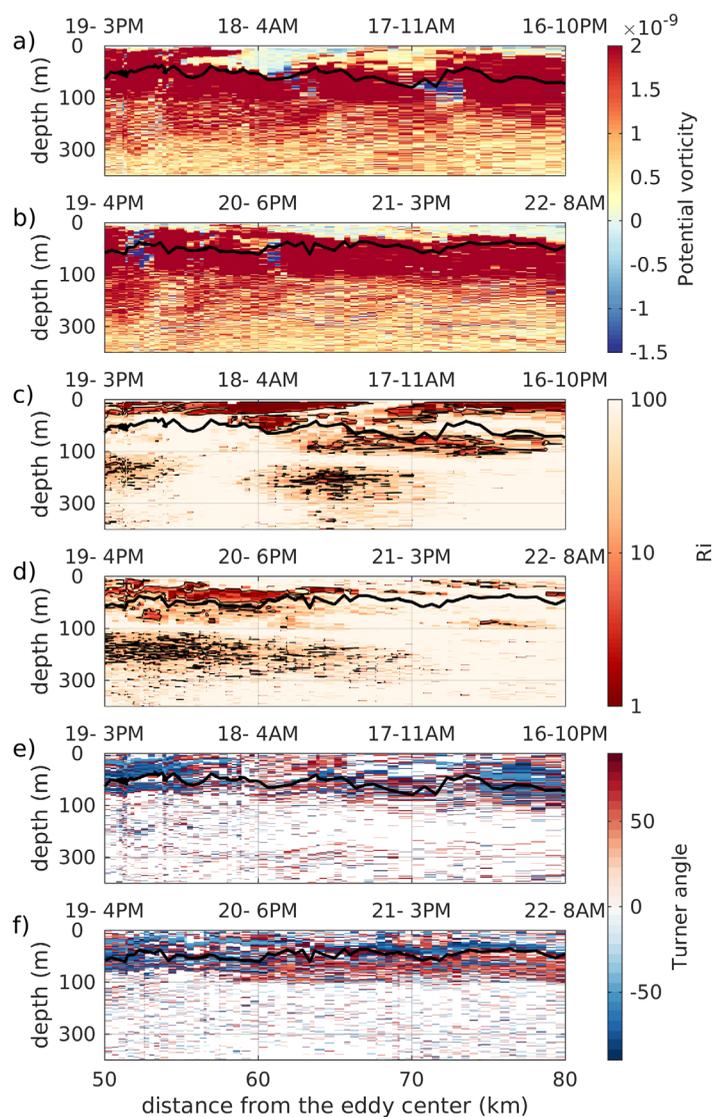
Figure 10. (a and b) geostrophic potential vorticity (s⁻²), (c and d) Richardson number (plotted on a log scale; black contour shows $Ri = 10$), and (e and f) Turner angle, derived from the glider data for the two crossings of the eddy rim from 16 to 22 March 2010 (the day of March and the time are indicated on top of the sections). The black thick line represents the depth of the mixed layer. Note that the vertical scale is not linear and highlights the 0–100 m part.

seem to originate from a region of high PV and reach toward the low PV core of the eddy, possibly indicating the future decay of the eddy through the removal of the anomalously low PV in the core.

4.2. Mesoscale Stirring

Several studies recently focused on the presence of layering outside of Mediterranean water eddies (Meddies), which are SCVs but at depth below 1,000 m. In particular, Meunier et al. (2015) investigated the role of stirring by the mean flow as a process that could generate sharp tracer gradients at the periphery of Meddies. They showed from a numerical simulation that a vertically sheared azimuthal flow can create density compensated filamentation in temperature and salinity on the side of a baroclinic eddy, e.g., a Meddie. This happens through differential advection that drives a direct cascade of vertical variance from large to small scales (Haynes & Anglade, 1997; Klein et al., 2008). The localization of this layering is preferentially in the immediate vicinity of critical layers of baroclinic instability where diffusion and dissipation is increased (Hua et al., 2013). Such layers are characterized by extrema of PV (Nguyen et al., 2012).

The fine scale structures in salinity and temperature that are few tens of meters thick and tilted toward the eddy rotational center underneath the low PV core are observed in the glider property data but not reproduced in the glider density field (Figures 6a and 6b). The vertically sheared vortex circulation characteristic of this SCV, along with the contrasted water masses observed inside and outside of the eddy, are conditions that can lead to the creation of fine scale density compensated structures (Klein et al., 1998; Smith & Ferrari, 2009). Spiciness S (Munk, 1981; Veronis, 1972), as a passive tracer, can show the presence of such formations. It is defined as $S = \alpha T' + \beta S'$, where α is the thermal expansion coefficient, β the saline contraction coefficient and the primes indicate deviation from the mean. Strong variability in spiciness not associated with variability in density is an indicator of density compensating effects. The glider spiciness field exhibits vertical small-scale variability between 100 and 400 m depth (Figure 11). Vertical profiles of spiciness and density anomalies show important differences (Figure 11c) that highlight the much stronger variability of the former compare to the latter. This suggests that tracer stirring may be an important process in the region. The presence of sharp PV jumps in the mixed layer (Figures 9a, 10a, and 10b), linked with horizontal variability of the current field, also suggest that critical-level of instability could play a role in the location of the layering around the eddy (Hua et al., 2013; Nguyen et al., 2012).

Geostrophic eddy stirring generates filaments with an aspect ratio proportional to f/N (Smith & Ferrari, 2009). Though a substantial scatter is expected around this value. The observed intrusions have length scales of about 10–20 km with vertical extension of 10–50 m and yield a ratio of vertical to horizontal scales ranging from 5×10^{-4} to 5×10^{-3}. Note that because of the 2-D nature of the data set, the horizontal extension of those features is probably underestimated. The squared root of the averaged Brunt-Väisälä frequency ranges from 17×10^{-3} in the mixed layer to 4×10^{-3} in the interior making f/N comprised between 2.5×10^{-3} and 1×10^{-2}. Although both intervals have some overlap, the intrusions appear to have aspect ratio smaller than f/N suggesting other mechanisms could also be at work around the eddy.

4.3. Diapycnal Mixing

Mixing processes can halt the variance cascade at small scale and play a crucial role in shaping the intrusions. It is possible that the observed thermohaline variability results from the combined action of lateral
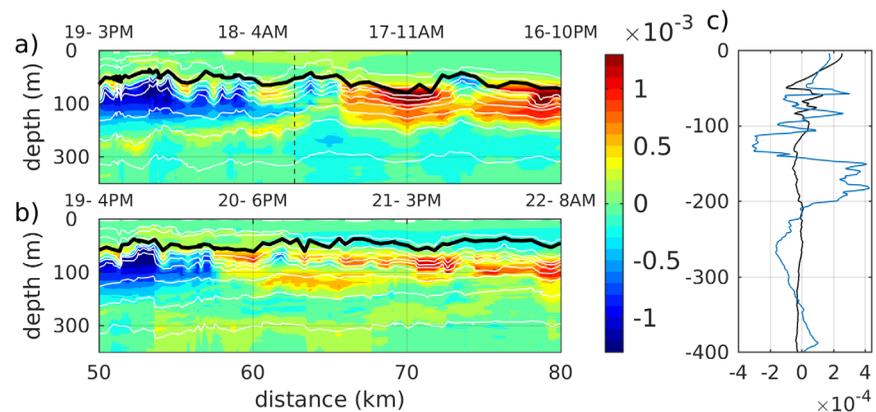
Figure 11. Glider spice anomaly from 16 to 22 March 2010 (the day of March and the time are indicated on top of the sections). Whites lines represent isopycnals and the black thick line the mixed layer base. Note that the vertical scale is not linear to highlights the 0–100 m part. (c) Vertical profile of spice (blue) and density anomaly ρ'/ρ_0 (black) at 62 km from the eddy center (dashed vertical line in the section a).

stirring, submesoscale instabilities and vertical mixing at small scales (Song et al., 2011). Two processes have been shown to dissipate tracer variance and favor diapycnal fluxes: turbulent mixing and double-diffusive convective mixing. In this section we will investigate the action of double-diffusion and NIW breaking on the periphery of the eddy.

Double-diffusive processes act at the molecular level and the tracer variance inversely cascades up to the submesoscales. It can lead to the creation of fine scale interleaving features such as the ones observed along the glider section or enhance already existing vertical T/S gradients. The Turner angle (Tu; Ruddick, 1983),

$$Tu = \tan^{-1} \frac{\alpha \partial T/\partial z - \beta \partial S/\partial z}{\alpha \partial T/\partial z + \beta \partial S/\partial z}$$

indicates susceptibility of the flow to double diffusion through salt fingering or diffusive convection. Tu was calculated at the mooring site and along the glider tracks (Figures 9b, 10e, and 10f). Both data sets show that the flow is prone to diffusive convection ($Tu < -45°$) and salt fingering ($Tu > 45°$) in the mixed layer while generally stable below with a few exceptions. Two regions above and below the upper low PV core of the eddy, at ∼40 m depth and ∼75 m depth, and on the periphery, between 50 and 80 m depth (Figure 9b) show indications of high susceptibility to salt fingering. The high vertical resolution of the glider measurements (∼1–2 m) should more accurately highlight the regions prone to present double-diffusive processes. Below the mixed layer, however, very few data points show Turner angles superior to 45° or inferior to −45° (Figures 10e and 10f). Moreover, double-diffusive interleaving can be affected by the baroclinicity of the flow.

May and Kelley (1997) compared intrusions slopes with cross-front salinity and density gradients and argued that shear may either increase or decrease growth rates of double-diffusive instabilities. They defined a maximum slope for the interleaving layers above which the baroclinic instability likely suppress the effect of double diffusion,

$$s_{max} = \frac{e_z \bar{S}_x/\bar{S}_z + \bar{\rho}_x/\bar{\rho}_z}{e_z + 1},$$

where the subscripts x and z are the radial and vertical derivatives, respectively, and the overbar represent the background flow. The nondimensional quantity ε_z is defined as $e_z = -(1 - \gamma_f)\beta \bar{S}_z/(\bar{\rho}_z/\rho_0)$ where γ_f is the flux ratio for salt fingering ($\gamma_f = 0.7$, McDougall & Ruddick, 1992). Using the two typical T/S profiles defined section 3.4.2 for the water masses inside and outside of the eddy (Figure 4) to derive the salinity and density gradients of the background flow, the maximum slope is $s_{max} \sim 5 \times 10^{-4}$. The observed features slope more steeply (5×10^{-4} to 5×10^{-3}) than theoretical predictions and observations for growing thermohaline intrusions (May & Kelley, 1997), therefore, even though double-diffusive processes could be active in the layering region, their growth is probably halted.
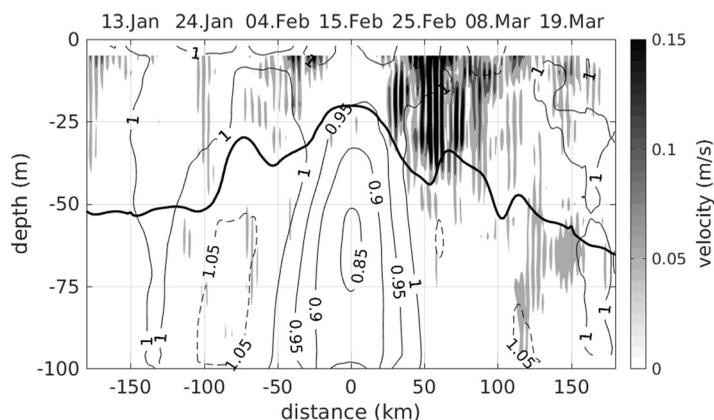
Figure 12. Near-inertial current amplitude ($(u^2 + v^2)^{1/2}$) at the mooring site calculated from band-pass filtered ADCP velocities from 10 January to 22 March 2010. Black contours represents f_{eff}/f. The thick black line shows the depth of the mixed layer.

Diapycnal mixing in the ocean interior is often associated with breaking of internal waves. Anticyclonic eddies are also known to concentrate near-inertial motions with slightly subinertial frequencies that can play an important role in vertical mixing (e.g., Alford et al., 2016). Negative vorticity in an anticyclone locally broaden the internal wave band by shifting the lower bound of the internal wave from the local planetary frequency (f) to an effective frequency $f_{eff} = f + \zeta/2$ (e.g., Kunze, 1985). Vertical waves propagating into a region of $f_{eff} < f$ become superinertial and the internal wave energy density is reduced compared to the f region. In contrast, in a region with $f_{eff} > f$, the spectrum is narrowed, energy density increases and the energy propagation slows down. Anticyclonic eddies are associated with a negative vorticity and show a $f_{eff} < f$ in their core (which equals to $\zeta/f < 0$, Figure 5a), however, in the transition outward from the velocity maximum toward the (stagnant) background flow a $\zeta > 0$ is created (Figure 5a) and as such $f_{eff} > f$ and trapping of waves is possible with high vertical velocity shear and a subsequent impact on turbulent diffusion (Byun et al., 2010; Halle & Pinkel, 2003; Kawaguchi et al., 2016; Ledwell et al., 2008; Lee & Niiler, 1998). In addition, expending on the work by Whitt and Thomas (2013), Joyce et al. (2013) showed how NIW within a baroclinic vortex can achieve minimum frequency even below f_{eff}. The minimum inertial frequency can be reduced to $f_{min} = \sqrt{f_{eff}^2 - f^2 Ri^{-1}}$ where the baroclinicity of the flow is expressed through the Richardson number. Regions of reduced Ri can allow a trapping mechanism for NIWs that can lead to the generation of critical layers, wave breaking, and enhanced mixing as shown for Warm Core eddies (Joyce et al., 2013). Using the direct observation of velocity available from the moored ADCP, that only sampled the first 100 m of the water column, the NIW energy, expressed here as the velocity magnitude in the NIW frequency spectrum (0.8f to 1.2f), was estimated (Figure 12). We found energy peaks at the edges of the eddy and which reached below the mixed layer at the downwind edges of the eddy and lasted for more than 14 days (20 February to 5 March). Inspecting the wind time series (Figure 2a) no related wind variability was found although the wind varies with a period of ∼13 days with at least four relatively high wind events (∼10 m/s) observed during the passing of the eddy by the mooring site. Moreover, the eddy core below the mixed layer was free of NIW. These findings are in agreement with other studies (Halle & Pinkel, 2003; Kawaguchi et al., 2016; Sheen et al., 2015) and explained by the rapid vertical propagation of NIW through the low PV core. The values of $Ri(O(1–10))$ observed at the eddy periphery suggest that the trapping and breaking of NIW is possible and could play a role in the mixing of properties in those regions. In fact, Karstensen et al. (2017) analyzed high-resolution ship based velocity data and CTD based stratification profiles from a SCV in the eastern tropical North Atlantic in many respects comparable to the one discussed here. They reported on dynamical features consistent with the vertical propagation of NIW at the outer rim of the SCV, but also at the mixed layer base, creating gradient Richardson numbers that indicate the existence of critical shear driven mixing. The NIW showed wave length similar to the intrusions we observed and since layering is known to occur favorably in regions where diffusion is increased, the presence of near-inertial critical layers at the periphery of the eddy would corroborate that this region is conducive to small-scale intrusions. However, further targeted observational studies would be required to verify this hypothesis.

5. Conclusions

Direct observations of a SCV originating from the coast of Mauritania were acquired in the eastern North Atlantic in February and March 2010 by two different observing platforms: a mooring and a glider, about ∼100 km and 1 month apart, both revealed the complex structure of the eddy. The eddy by chance crossed the mooring with its center and thus a unique time series of stratification and direct velocity measurements (upper 100 m only) have been acquired. Mooring and glider data, along with satellite observations of SLA, surface winds, and chlorophyll surface concentration, allowed us to provide a detailed picture of the eddy as well as highlight elusive features that define SCVs in the open ocean.

Our in situ observations reveal a well-isolated core with a very low PV and homogenous T/S properties of SACW origin typically found in the undercurrent along the eastern boundary upwelling region. The SCV core also showed very low oxygen concentrations as has been reported before for this SCV (Karstensen et al., 2015) and other SCVs in the region (Karstensen et al., 2017; Schütte et al., 2016b). Inspecting ocean color derived chlorophyll satellite images indicates the high productivity inside and around the eddy core which in turn suggests upwelling of nutrient-rich water.

The SCV had a radius of ∼50 km and a maximum rotational speed of ∼0.4 m s^{-1} at ∼80 m depth. The vortex characteristic Burger number was 0.2 and the vortex Rossby number 0.15, suggesting a balanced flat lens eddy. Note that the vorticity locally reached a maximum of ∼0.3 f. Above the low PV core the isopycnals were dome-shaped and below they were bowl-shaped. The eddy influence can be observed up to at least 1,000 m depth. On the rim of this eddy fine scale variability was highlighted with features presenting horizontal scales (O(10 km)) and vertical extensions of tens of meters. In particular, the glider observations revealed relatively salty and oxygenated features between 100 and 350 m depth.

The fine scale variability on the periphery along with the patchiness of the surface chlorophyll concentration lead us to investigate a number of destabilizing processes that could lead to submesoscale vertical variability that may ultimately supply nutrient transport into the euphotic zone. First, symmetric instability can drive radial secondary circulations in anticyclonic eddies (Brannigan, 2016). Localized regions where the PV was very low, and even negative, in the surface layer suggest a susceptibility of the flow to this instability that could be responsible for the upwelling of nutrient in the mixed layer around the eddy, which would be consistent with the observed chlorophyll concentration on the surface. However, below the mixed layer the eddy is mostly symmetrically stable which indicates that another process must drive the small-scale variability in salt and oxygen. Second, differential stirring by 3-D turbulence along sloping isopycnals of existing large scale gradients can drive a cascade of variance toward small scale and generate layering in the vertical with scales similar to the one observed around the eddy (Meunier et al., 2015). The saline and oxygenated intrusions sloping toward the center of the eddy in subsurface could thus be the signature of interleavings that may play a role in the long-term decay of the eddy.

The lateral stirring of T/S properties around the eddy might make the flow susceptible to secondary instabilities that can trigger diapycnal mixing. In particular, double-diffusive instabilities can appear along T/S filaments. However, as the slope of the interleaving layers indicates, the baroclinic character of the SCV would tend to inhibit this process. Furthermore, SCVs are baroclinic anticyclonic eddies with a negative relative vorticity in the core and positive vorticity at the rim. The modification of the planetary vorticity felt by near-inertial gravity wave (NIGW) has been shown to favor their trapping. Wind driven near-inertial motions are very likely to occur in the vicinity of eddied such as this one and they would enhance mixing in particular in regions where the baroclinicity is important (Halle & Pinkel, 2003; Kawaguchi et al., 2016). As such we expect that on the rim of the eddy vertical mixing would be strong and favor vertical fluxes (Karstensen et al., 2017).

Here we showed that the dynamics of the eddy would allow several types of processes to be at work. In particular, through the careful observation of the diverse data sets we conclude that isopycnal eddy stirring can explain the observed thermohaline filaments on the rim where enhanced mixing, that could be due to NIW induced shear and eventually breaking, should also play a role. In the highly energetic environment surrounding a mesoscale eddy, it is likely that many processes are competing. Note that the observed variability could also be the remnant of former advective events that would not have been diffused yet. Progress toward identifying and discriminating definitely between the processes able to generate such small-scale filamentation in an SCV would require investigation in a full 3-D framework through dedicated observation campaigns and high-resolution modeling to provide a better understanding of the physical and biogeochemical coupling.

References

Alford, M. H., MacKinnon, J. A., Simmons, H. L., & Nash, J. D. (2016). Near-inertial internal gravity waves in the Ocean. *Annual Review of Marine Science*, 8(2016), 95–123. https://doi.org/10.1146/annurev-marine-010814-015746

Armi, L., Hebert, D., Oakey, N., Price, J., Richardson, P. L., Rossby, T., et al. (1988). The history and decay of a Mediterranean Salt Lens. *Nature*, 333, 649–651.

Armi, L., & Zenk, W. (1984). Large lenses of highly saline Mediterranean water. *Journal of Physical Oceanography*, 14, 1560–1576.

Bentamy, A., & Croize-Fillon, D. (2011). Gridded surface wind fields from Metop/ASCAT measurements. *International Journal of Remote Sensing*, *8*, 1–26.

Bosse, A., Testor, P., Mortier, L., Prieur, L., Taillandier, V., D'ortenzio, F., et al. (2015). Spreading of Levantine Intermediate Waters by submesoscale coherent vortices in the northwestern Mediterranean Sea as observed with gliders. *Journal of Geophysical Research: Oceans*, *120*, 1599–1622. https://doi.org/10.1002/2014JC010263

Brannigan, L. (2016). Intense submesoscale upwelling in anticyclonic eddies. *Geophysical Research Letters*, *43*, 3360–3369. https://doi.org/10.1002/2016GL067926

Byun, S.-S., Park, J. J., Chang, K.-I., & Schmitt, R. W. (2010). Observation of near-inertial wave reflections within the thermostad layer of an anticyclonic mesoscale eddy. *Geophysical Research Letters*, *37*, L01606. https://doi.org/10.1029/2009GL041601

Chaigneau, A., LeTexier, M., Eldin, G., Grados, C., & Pizarro, O. (2011). Vertical structure of mesoscale eddies in the eastern South Pacific Ocean: A composite analysis from altimetry and Argo profiling floats. *Journal of Geophysical Research: Oceans*, *116*, C07002. https://doi.org/10.1029/2011JC007134

Chelton, D. B., Gaube, P., Schlax, M. G., Early, J. J., & Samelson, R. M. (2011). The influence of nonlinear mesoscale eddies on near-surface oceanic chlorophyll. *Science*, *334*, 328–332.

Colas, F., McWilliams, J., Capet, X., & Kurian, J. (2012). Heat balance and eddies in the Peru-Chile current system. *Climate Dynamics*, *39*, 509–529.

d'Asaro, E. (1988). Generation of submesoscale vortices: A new mechanism. *Journal of Geophysical Research*, *93*, 6685–6693.

D'Asaro, E., Walker, S., & Baker, E. (1994). Structure of two hydrothermal megaplumes. *Journal of Geophysical Research: Oceans*, *99* (C10), 20361–20373.

Dewar, W. K., & Flierl, G. R. (1987). Some effects of the wind on rings. *Journal of Physical Oceanography*, *17*, 1653–1667.

Fan, X., Send, U., Testor, P., Karstensen, J., & Lherminier, P. (2013). Observations of Irminger Sea anticyclonic eddies. *Journal of Physical Oceanography*, *43*, 805–823. https://doi.org/10.1175/JPO-D-11-0155.1

Flierl, G. R. (1981). Particle motions in large-amplitude wave fields. *Geophysical & Astrophysical Fluid Dynamics*, *18*, 39–74. https://doi.org/10.1080/03091928108208773

Fukumori, I. (1992). Meridional circulation and mixing associated with the decay of warm-core ring 82B. *Deep Sea Research, Part A*, *39*(suppl. 1), S45–S65.

Garfield, N., Collins, C. A., Paquette, R. G. & Carter E. (1999). Lagrangian exploration of the California Undercurrent 1992–95. *Journal of Physical Oceanography*, *29*, 560–583.

Garau, B., Ruiz, S., Zhang, W. G., Pascual, A., Heslop, E., Kerfoot, J., et al. (2011). Thermal lag correction on Slocum CTD glider data. *Journal of Atmospheric and Oceanic Technology*, *28*, 1065–1071.

Godø, O. R., Samuelsen, A., Macaulay, G. J., Patel, R., Hjøllo, S., Horne, J., et al. (2012). Mesoscale eddies are oases for higher trophic marine life. *PLoS ONE*, *7*(1), e30161. https://doi.org/10.1371/journal.pone.0030161

Hahn, J., Brandt, P., Greatbatch, R. J., Krahmann, G., & Körtzinger, A. (2014). Oxygen variance and meridional oxygen supply in the Tropical North East Atlantic oxygen minimum zone. *Climate Dynamics*, *43*, 2999–3024.

Halle, C., & Pinkel, R. (2003). Internal wave variability in the Beaufort Sea during the winter of 1993/1994. *Journal of Geophysical Research*, *108*(C7), 3210. https://doi.org/10.1029/2000JC000703

Haynes, P. H., & Anglade, J. (1997). The vertical-scale cascade of atmospheric tracers due to large-scale differential advection. *Journal of Atmospheric Sciences*, *54*, 1121–1136.

Hebert, D., Oakey, N., & Ruddick, B. (1990). Evolution of a Mediterranean salt lens: Scalar properties. *Journal of Physical Oceanography*, *20*, 1468–1483. https://doi.org/10.1175/1520-0485

Hormazabal, S., Combes, V., Morales, C. E., Correa-Ramirez, M. A., Di Lorenzo, E., & Nuñez, S. (2013). Intrathermocline eddies in the coastal transition zone off central Chile (31–41°S). *Journal of Geophysical Research*, *118*, 4811–4821. https://doi.org/10.1002/jgrc.20337

Hua, B. L., Ménesguen, C., Le Gentil, S., Schopp, R., Marsset, B., & Aiki, H. (2013). Layering and turbulence surrounding an anticyclonic oceanic vortex: In situ observations and quasi-geostrophic numerical simulations. *Journal of Fluid Mechanics*, *731*, 418–442.

Joyce, T. M. (1977). A note on the lateral mixing of water masses. *Journal of Physical Oceanography*, *7*, 626–629. https://doi.org/10.1175/1520-0485(1977)007<0626:ANOTLM>2.0.CO;2

Joyce, T. M., & McDougall, T. J. (1992). Physical structure and temporal evolution of Gulf Stream warm-core ring 82B. *Deep Sea Research, Part A*, *39*(suppl. 1), S19–S44.

Joyce, T. M., Toole, J. M., Klein, P., & Thomas, L. N. (2013). A near-inertial mode observed within a Gulf Stream warm-core ring. *Journal of Geophysical Research: Oceans*, *118*, 1797–1806. https://doi.org/10.1002/jgrc.20141

Karstensen, J., Fiedler, B., Schütte, F., Brandt, P., Körtzinger, A., Fischer, G., et al. (2015). Open ocean dead zones in the tropical North Atlantic Ocean. *Biogeosciences*, *12*, 2597–2605. https://doi.org/10.5194/bg-12-2597-2015

Karstensen, J., Schütte, F., Pietri, A., Krahmann, G., Fiedler, B., Grundle, D., et al. (2017). Upwelling and isolation in oxygen-depleted anticyclonic modewater eddies and implications for nitrate cycling. *Biogeosciences*, *14*, 2167–2181. https://doi.org/10.5194/bg-14-2167-2017

Kawaguchi, Y., Nishino, S., Inoue, J., Maeno, K., Takeda, H., & Oshima, K. (2016). Enhanced diapycnal mixing due to near-inertial internal waves propagating through an anticyclonic eddy in the ice-free Chukchi Plateau. *Journal of Physical Oceanography*, *46*, 2457–2481. https://doi.org/10.1175/JPO-D-15-0150.1

Klein, P., Hua, B. L., Lapeyre, G., Capet, X., Gentil, S. L., & Sasaki, H. (2008). Upper ocean turbulence from high-resolution 3D simulations. *Journal of Physical Oceanography*, *38*, 1748–1763.

Klein, P., & Lapeyre, G. (2009). The oceanic vertical pump induced by mesoscale and submesoscale turbulence. *Annual Review of Marine Science*, *1*, 351–375.

Klein, P., Treguier, A. M., & Hua, B. L. (1998). Three-dimensional stirring of thermohaline fronts. *Journal of Marine Research*, *56*, 589–612. https://doi.org/10.1357/002224098765213595

Kunze, E. (1985). Near-inertial wave propagation in geostrophic shear. *Journal of Physical Oceanography*, *15*, 544–565.

Kunze, E., Schmitt, R. W., & Toole, J. M. (1995). The energy balance in a Warm-Core Ring's near-inertial critical layer. *Journal of Physical Oceanography*, *25*, 942–957.

Ledwell, J. R., McGillicuddy, D., Jr., & Anderson, L. (2008). Nutrient flux into an intense deep chlorophyll layer in a mode-water eddy. *Deep Sea Research, Part II*, *55*, 1139–1160. https://doi.org/10.1016/j.dsr2.2008.02.005

Ledwell, J. R., Watson, A. J., & Law, C. S. (1993). Evidence of slow mixing across the pycnocline from an open-ocean tracer-release experiment. *Nature*, *364*, 701–703.

Lee, D.-K., & Niiler, P. P. (1998). The inertial chimney: The near-inertial energy drainage from the ocean surface to the deep layer. *Journal of Geophysical Research*, *103*, 7579–7591.

Lilly, J., & Rhines, P. (2002). Coherent eddies in the Labrador Sea observed from a mooring. *Journal of Physical Oceanography*, *32*, 585–598.

Lilly, J., Rhines, P., Schott, F., Lavender, K., Lazier, J., Send, U., & D'Asaro, E. (2003). Observations of the Labrador Sea eddy field. *Journal of Physical Oceanography*, *59*, 75–176.

Mahadevan, A., & Archer, D. (2000). Modeling the impact of fronts and mesoscale circulation on the nutrient supply and biochemistry of the upper ocean. *Journal of Geophysical Research*, *105*, 1209–1225.

Mahadevan, A., & Tandon, A. (2006). An analysis of mechanisms for submesoscale vertical motion at ocean fronts. *Ocean Modelling*, *14*, 241–256.

Martin, A. P., & Richards, K. J. (2001). Mechanisms for vertical nutrient transport within a North Atlantic mesoscale eddy. *Deep Sea Research, Part II*, *48*, 757–773.

May, B. D., & Kelley, D. E. (1997). Effect of baroclinicity on double-diffusive interleaving. *Journal of Physical Oceanography*, *27*, 1997–2008.

McDougall, T. J., & Ruddick, B. R. (1992). The use of ocean microstructure to quantify both turbulent mixing and salt-fingering. *Deep Sea Research, Part A*, *39*(11–12), 1931–1952.

McGillicuddy, D. J., Anderson, L. A., Bates, N. R., Bibby, T., Buesseler, K. O., Carlson, C. A., et al. (2007). Eddy/wind interactions stimulate extra-ordinary mid-ocean plankton blooms. *Science*, *316*, 1021– 1026. https://doi.org/10.1126/science.1136256

McWilliams, J. C. (1985). Submesoscale, coherent vortices in the ocean. *Reviews of Geophysics*, *23*, 165–182. doi:10.1029/RG023i002p00165

McWilliams, J. C. (2016). Submesoscale currents in the ocean. *Proceedings of the Royal Society of London A*, *472*, 20160117. https://doi.org/10.1098/rspa.2016.0117

Meunier, T., Ménesguen, C., Schopp, R., & Gentil, S. L. (2015). Tracer stirring around a meddy: The formation of layering. *Journal of Physical Oceanography*, *45*, 407–423. https://doi.org/10.1175/JPO-D-14-0061.1

Molemaker, M. J., McWilliams, J. C., & Dewar, W. K. (2015). Submesoscale instability and generation of mesoscale anticyclones near a separation of the California undercurrent. *Journal of Physical Oceanography*, *45*, 613–629. https://doi.org/10.1175/JPO-D-13-0225.1

Munk, W. (1981). Internal waves and small-scale processes. In B. A. Warren & C. Wunsch (Eds.), *Evolution of physical oceanography: Scientific surveys in honor of Henry Stommel* (pp. 264–291). Cambridge, MA: MIT Press.

Nguyen, H. Y., Hua, B. L., Schopp, R., & Carton, X. (2012). Slow quasigeostrophic unstable modes of a lens vortex in a continuously stratified flow. *Geophysical & Astrophysical Fluid Dynamics*, *106*, 305–319. https://doi.org/10.1080/03091929.2011.620568

Pelland, N. A., Eriksen, C. C., & Lee, C. M. (2013). Subthermocline eddies over the Washington Continental slope as observed by seagliders, 2003-09. *Journal of Physical Oceanography*, *43*, 2025–2053.

Pietri, A., Echevin, V., Testor, P., Chaigneau, A., Mortier, L., Grados, C., et al. (2014). Impact of a coastal-trapped wave on the near-coastal circulation of the Peru upwelling system from glider data. *Journal of Geophysical Research: Oceans*, *119*, 2109–2120. https://doi.org/10.1002/2013JC009270

Pietri, A., Testor, P., Echevin, V., Chaigneau, A., Mortier, L., Eldin, G., et al. (2013). Finescale vertical structure of the upwelling system off southern Peru as observed from glider data. *Journal of Physical Oceanography*, *43*, 631–646.

Pingree, R. D., & Le Cann, B. (1993). Structure of a meddy (Bobby 92) southeast of the Azores. *Deep Sea Research, Part I*, *40*, 2077–2103. https://doi.org/10.1016/0967-0637(93)90046-6

Ruddick, B. (1983). A practical indicator of the stability of the water column to double-diffusive activity. *Deep Sea Research, Part A*, *30*, 1105–1107.

Ruddick, B. (1992). Intrusive mixing in a Mediterranean salt lens—Intrusion slopes and dynamical mechanisms. *Journal of Physical Oceanography*, *22*, 1274–1285. https://doi.org/10.1175/1520-0485

Ruddick, B., & Hebert, D. (1988). The mixing of Meddy Sharon. In J. C. J. Nihoul & B. M. Jamart (Eds.), *Small-scale turbulence and mixing in the ocean. Elsevier oceanography series* (Vol. 46, pp. 249–261). New York, NY: Elsevier. https://doi.org/10.1016/S0422-9894(08)70551-8

Ruddick, B. R., & Walsh, D. (1994). Observations of density perturbations which drive thermohaline intrusions. In A. Brandt & H. Fernando (Eds.), *Double-diffusive convection, Geophysical Monograph Series* (Vol. 94, pp. 329–334). Washington, DC: American Geophysical Union.

Sackmann, B. S., Perry, M. J., & Ericksen, C. C. (2008). Seaglider observations of variability in daytime fluorescence quenching of chlorophyll-a in Northeastern Pacific coastal waters. *Biogeosciences Discussion*, *5*, 2839–2865.

Samuelsen, A., Hjøllo, S. S., Johannessen, J. A., & Patel, R. (2012). Particle aggregation at the edges of anticyclonic eddies and implications for distribution of biomass. *Ocean Science*, *8*, 389–400. https://doi.org/10.5194/os-8-389-2012

Schütte, F., Brandt, P., & Karstensen, J. (2016a). Occurrence and characteristics of mesoscale eddies in the tropical northeastern Atlantic Ocean. *Ocean Science*, *12*, 663–685. https://doi.org/10.5194/os-12-663-2016

Schütte, F., Karstensen, J., Krahmann, G., Hauss, H., Fiedler, B., Brandt, P., et al. (2016b). Characterization of ''dead-zone'' eddies in the eastern tropical North Atlantic. *Biogeosciences*, *13*, 5865–5881. https://doi.org/10.5194/bg-13-5865-2016

Shcherbina, A. Y., Sundermeyer, M. A., Kunze, E., D'Asaro, E., Badin, G., Birch, D., et al. (2015). The LatMix summer campaign: Submesoscale stirring in the upper ocean. *Bulletin of the American Meteorological Society*, *96*(8), 1257–1279. https://doi.org/10.1175/BAMS-D-14-00015.1

Sheen, K. L., Brearley, J. A., Naveira Garabato, A. C., Smeed, D. A., St Laurent, L., Meredith, M. P., et al. (2015). Modification of turbulent dissipation rates by a deep Southern Ocean eddy. *Geophysical Research Letters*, *42*, 3450–3457. https://doi.org/10.1002/2015GL063216

Smith, K. S., & Ferrari, R. (2009). The production and dissipation of compensated thermohaline variance by mesoscale stirring. *Journal of Physical Oceanography*, *39*, 2477–2501. https://doi.org/10.1175/2009JPO4103.1

Song, H., Pinheiro, L. M., Ruddick, B., & Teixeira, F. C. (2011). Meddy, spiral arms, and mixing mechanisms viewed by seismic imaging in the Tagus Abyssal Plain (SW Iberia). *Journal of Marine Research*, *69*, 4–6. https://doi.org/10.1357/002224011799849309

Stramma, L., Johnson, G. C., Sprintall, J., & Mohrholz, V. (2008). Expanding oxygen-minimum zones in the tropical oceans. *Science*, *320*, 655–658.

Thomas, L. N. (2005). Destruction of potential vorticity by winds. *Journal of Physical Oceanography*, *35*(12), 2457–2466.

Thomas, L. N., Tandon, A., & Mahadevan, A. (2008). Submesoscale processes and dynamics. In M. W. Hecht & H. Hasumi (Eds.), *Ocean modeling in an eddying regime, Geophysical Monograph Series* (Vol. 117, pp. 17–38). Washington, DC: American Geophysical Union. https://doi.org/10.1029/177GM04

Thomsen, S., Kanzow, T., Krahmann, G., Greatbatch, R. J., Dengler, M., & Lavik, G. (2015). The formation of a subsurface anticyclonic eddy in the Peru-Chile Undercurrent and its impact on the near- coastal salinity, oxygen and nutrient distributions. *Journal Geophysical Research: Oceans*, *121*, 476–501. https://doi.org/10.1002/2015JC010878

Todd, R. E., Rudnick, D. L., & Davis, R. E. (2009). Monitoring the greater San Pedro Bay region using autonomous underwater gliders during fall of 2006. *Journal of Geophysical Research*, *114*, C06001. https://doi.org/10.1029/2008JC005086

Veronis, G. (1972). Properties of seawater defined by temperature, salinity, and pressure. *Journal of Marine Research*, *30*, 227–255.

Whitt, D. B., & Thomas, L. N. (2013). Near-inertial waves in strongly baroclinic currents. *Journal of Physical Oceanography*, *43*(4), 706–725. https://doi.org/10.1175/JPO-D-12-0132.1

Yoshikawa, Y., Akitomo, K., & Awaji, T. (2001). Formation process of intermediate water in baroclinic current under cooling. *Journal of Geophysical Research*, *106*, 1033–1051.

Zhang, W.-Z., Xue, H., Chai, F., & Ni, Q. (2015). Dynamical processes within an anticyclonic eddy revealed from Argo floats. *Geophysical Research Letters*, *42*, 2342–2350. https://doi.org/10.1002/2015GL063120

Zhang, Z., Zhang, Y., & Wang, W. (2017). Three-compartment structure of subsurface-intensified mesoscale eddies in the ocean. *Journal of Geophysical Research: Oceans*, *122*, 1653–1664. https://doi.org/10.1002/2016JC012376

Zhang, Z., Zhang, Y., Wang, W., & Huang, R. X. (2013). Universal structure of mesoscale eddies in the ocean. *Geophysical Research Letters*, *40*, 3677–3681. https://doi.org/10.1002/grl.50736